BNL-107668-2015-JA

NANO LETTERS

Subscriber access provided by BNL Research Library

Communication

Unveiling Surface Redox Charge Storage of Interacting Two-Dimensional Hetero-Nanosheets in Hierarchical Architectures

Qasim Mahmood, Min Gyu Kim, Sol Yun, Seong-Min Bak, Xiao-Qing Yang, Hyeon Suk Shin, Woo-Sik Kim, Paul V. Braun, and Ho Seok Park

Nano Lett., **Just Accepted Manuscript** • Publication Date (Web): 03 Mar 2015

Downloaded from http://pubs.acs.org on March 5, 2015

Just Accepted

"Just Accepted" manuscripts have been peer-reviewed and accepted for publication. They are posted online prior to technical editing, formatting for publication and author proofing. The American Chemical Society provides "Just Accepted" as a free service to the research community to expedite the dissemination of scientific material as soon as possible after acceptance. "Just Accepted" manuscripts appear in full in PDF format accompanied by an HTML abstract. "Just Accepted" manuscripts have been fully peer reviewed, but should not be considered the official version of record. They are accessible to all readers and citable by the Digital Object Identifier (DOI®). "Just Accepted" is an optional service offered to authors. Therefore, the "Just Accepted" Web site may not include all articles that will be published in the journal. After a manuscript is technically edited and formatted, it will be removed from the "Just Accepted" Web site and published as an ASAP article. Note that technical editing may introduce minor changes to the manuscript text and/or graphics which could affect content, and all legal disclaimers and ethical guidelines that apply to the journal pertain. ACS cannot be held responsible for errors or consequences arising from the use of information contained in these "Just Accepted" manuscripts.

ACS Publications
High quality. High impact.

Nano Letters is published by the American Chemical Society. 1155 Sixteenth Street N.W., Washington, DC 20036
Published by American Chemical Society. Copyright © American Chemical Society. However, no copyright claim is made to original U.S. Government works, or works produced by employees of any Commonwealth realm Crown government in the course of their duties.

Unveiling Surface Redox Charge Storage of Interacting Two-Dimensional Hetero-Nanosheets in Hierarchical Architectures

*Qasim Mahmood[1], Min Gyu Kim[2], Sol Yun[3], Seongmin Bak[4], Xiao-Qing Yang[4], Hyeon Suk Shin[5], Woo Sik Kim[1], Paul V. Braun[6], and Ho Seok Park[3]**

[1]Department of Chemical Engineering, College of Engineering, Kyung Hee University, 1 Seochon-dong, Giheung-gu, Yongin-si, Gyeonggi-do 446-701, Republic of Korea

[2]Beamline Research Division, Pohang Accelerator Laboratory, Pohang, Republic of Korea

[3]School of Chemical Engineering, Sungkyunkwan University (SKKU), Suwon 440-746, Republic of Korea

[4]Chemistry Department, Brookhaven National Laboratory, New York 11973, USA

[5]Interdisciplinary School of Green Energy and Low Dimensional Carbon Materials Center, Ulsan National Institute of Science and Technology(UNIST), UNIST-gil 50, Ulsan 689-798, Republic of Korea

[6]Department of Materials Science and Engineering Materials Research Laboratory and Beckman Institute, University of Illinois at Urbana-Champaign, Urbana, Illinois, 61801, USA

Corresponding author: phs0727@skku.edu (H. S. Park)

Abstract: Two-dimensional (2D) hetero-nanosheets are currently the focus of intense study due to the unique properties that emerge from the interplay between two low-dimensional nanomaterials with different properties. However, the properties and new phenomena based on the two 2D hetero-nanosheets interacting in a 3D hierarchical architecture have yet to be explored. Here, we unveil the surface redox charge storage mechanism of surface-exposed WS_2 nanosheets assembled in a 3D hierarchical heterostructure using *in-situ* synchrotron X-ray absorption and Raman spectroscopic methods. The surface dominating redox charge storage of WS_2 is manifested in a highly reversible and ultrafast capacitive fashion due to the interaction of hetero-nanosheets and the 3D connectivity of the hierarchical structure. In contrast, compositionally identical 2D WS_2 structures fail to provide a fast and high capacitance with different modes of lattice vibration. The distinctive surface capacitive behavior of 3D hierarchically structured hetero-nanosheets is associated with rapid proton accommodation into the in-plane W-S lattice (with the softening of the E_{2g} bands), the reversible redox transition of the surface-exposed intralayers residing in the electrochemically active 1T phase of WS_2 (with the reversible change in the interatomic distance and peak intensity of W-W bonds), and the change in the oxidation state during the proton insertion/deinsertion process. This proposed mechanism agrees with the dramatic improvement in the capacitive performance of the two hetero-nanosheets coupled in the hierarchical structure.

KEYWORDS: energy storage mechanism, redox reaction, 2D nanomaterial, hetero-nanosheet, in-situ spectroscopy, hierarchical structure

2D nanosheets such as graphene and dichalcogenides, characterized as weak van der Waals interactions between individual layers and strong in-plane bonding,[1] have been found to offer intriguing properties of large surface-to-volume ratio,[2] confined thickness on the atomic scale,[3] surface-dominated phenomena,[4] and unusual chemical reactivity.[5,6] As a new class of "artificial materials", 2D hetero-nanosheets are assembled with compositional variations by restacking individual layered materials that possess different yet complementary or synergistic properties.[7,8,9-11] The unique features of 2D hetero-nanosheets originating from the strong interlayer interactions between different nanosheets are exemplified by the emerging properties (e.g. ultrafast charge transfer between van der Waals-coupled layers and tunable optoelectronic properties)[12,13] and new physics (e.g. novel Vand Hove Singularities, superlattice Dirac points and Hofstadter butterfly pattern).[14-16] Notwithstanding recent important findings about the electronic coupling of 2D heterostructures for electronic and optoelectronic applications,[7-11] the emerging electrochemical properties of 2D hetero-nanosheets for energy storage are not observed yet. If hetero-nanosheets are used as building blocks for 3D hierarchical architectures, the resulting materials can have even more significant advantages including large contact areas and interplay of two nanosheets and quantum confinement by the 2D geometry[2-6] over the hierarchical heterostructures constructed by nanomaterials of different dimensions. Moreover, the hierarchically structured, 2D hetero-nanosheets can provide easy ion accessibility, percolated electron transport, and low-resistant ion diffusion as a consequence of the 3D continuous internetworks (e.g. graphene aerogels).[17,18] Accordingly, 2D hetero-nanosheets coupled in hierarchical, complex structures are hypothesized to generate synergistic and emerging functionalities that are otherwise difficult to realize with current, conventional technologies. Despite the aforementioned features, the co-assembly of 2D hetero-nanosheets into 3D macroscale architectures remains critically challenging due to the complexity of the necessary structures and the energetic and/or entropic penalties required for the re-assembly of a 2D geometry.[19,20] In particular, the unexpected properties and new phenomena of the 2D hetero-nanosheets interacting in a 3D hierarchical architecture have yet to be explored.

As a proof of concept, we chose reduced graphene oxide (RGO) and WS_2 or MoS_2 (as representative dichalcogenides) nanosheets as the 2D building blocks for our 3D macroscale architectures. It should be noted that the assembling chemistry suggested herein is not limited to this example but represents a generic approach that can be applied to other 2D nanomaterials. Taking full advantage of both RGO and WS_2 (or MoS_2) assembled in a hetero-compositional fashion[7-11] and synergizing the features of the 2D micro- and 3D macroscopic structures constructed in a hierarchical manner,[17,18,21] emerging properties that cannot be achieved with existing materials can be accomplished. In terms of its chemical identity, dichalcogenide is regarded as a promising redox-active material that stores charges *via* faradaic reactions;[22,23] therefore, it can overcome the critical shortcomings commonly found in double layer capacitive materials (including RGO) such as low capacitance.[24] However, power and cyclic capabilities can be deteriorated by the slow diffusion of redox charge carriers and the low electrochemical stability of dichalcogenides.[25,26] As a consequence of the sluggish ion kinetics and the low electronic conductivity of dichalcogenides that limit surface redox chemistry or pseudocapacitive behaviour,[27,28] there are very few reports about its application into electrochemical capacitors (ECs). Importantly, the surface charge storage mechanism of these materials is poorly understood on an atomic level, because most dichalcogenides and their composites have shown diffusion-controlled insertion mechanism.[23,26] Herein, we demonstrate for the first time the highly reversible and ultrafast capacitive features of surface-exposed WS_2 nanosheets interacting with RGOs in a 3D hierarchical heterostructure and the surface redox charge storage mechanism via *in-situ* synchrotron X-ray absorption and Raman spectroscopic techniques.

As illustrated by Figure 1, we devised a versatile method to construct 3D macroporous architectures assembled by 2D RGO/dichalcogenide hetero-nanosheets (see Supporting Information S1). For the well-defined hierarchical structure, 2D hetero-sheets must be uniformly dispersed in an aqueous solution (see Fig. S1 and Supporting Information S2). 2D nanosheets such as RGO, WS_2, and MoS_2 were exfoliated into either a single or a few layers (< 5 layers) through solution chemistry as previously reported.[29,30] The quality of the dichalcogenide nanosheets was confirmed (see Figs. S2, S3 and see

Supporting Information S3). The hetero-nanosheet dispersions were very stable due to the electrostatic repulsion forces generated by the negatively charged surfaces of the three nanosheets. At specific pHs (ranging from 6 to 8), negatively charged hetero-nanosheets were co-assembled with positively charged amine-modified PS beads; these beads act as templates through electrostatic interactions (see Supporting Information S4). As seen in the scanning electron microscopy (SEM) images (see Fig. S4), PS beads were covered by the hetero-nanosheets. After removing PS beads by solvent extraction, 3D macroporous RGO/WS_2 and RGO/MoS_2 hetero-nanosheets (designated as 3D RWhs and 3D RMhs, respectively) were successfully obtained without structural demolition (see Fig. S5). The macroscale pore sizes of 3D RWhs and 3D RMhs were in the range of 100 nm – 1 μm and were readily controlled by varying the diameters of the PS beads (see Fig. S4). The hetero-compositions were manipulated by controlling the initial mixing ratios of RGO and dichalcogenide. Furthermore, hierarchical homo-nanosheets such as 3D GO, RGO, MoS_2, and WS_2 were readily synthesized using the same method (see Fig. S5). This strategy of combining colloidal and template chemistries offers a facile and versatile synthetic method to fabricate 3D macroporous architectures assembled by 2D hetero-nanosheets.

The morphologies of 3D RWhs were analyzed using SEM, transmission electron microscopy (TEM), and scanning TEM (STEM) as shown in Figure 2. Examination of the RWhs with SEM revealed 3D interconnected macroporous structures, where the pore walls were composed of RGO and WS_2 nanosheets (Figs. 2a, 2b). The macropores in 3D RWhs had a diameter of ~1 μm, which is consistent with the size of PS beads used as templates. Furthermore, ~30 nm mesopores originating from the intervoids of hetero-sheets were verified by N_2 sorption/desorption analysis with a surface area of 21.2 m^2/g and a pore volume of 0.183 cm^3/g (see Table S1). Notably, the existence of macroporosity was supported by the contrast differences between the pore and the wall as shown in TEM and high-angle annular dark field scanning TEM (HAADF-STEM) images (Figs. 2c, 2e). The fringed lattice observed by high resolution TEM (HR-TEM) and the corresponding fast Fourier transform (FFT) pattern indicate the nanocrystalline structure of a few layers of WS_2 (Fig. 2d). The interplanar spacing of 2.3 Å in the WS_2 domains corresponds to the (103) planes of the XRD spectra (see Fig. S3). Both the

hetero-compositions and the random distributions of 3D RWhs were substantiated by carbon, sulphur, and tungsten elemental mappings using energy-dispersive spectroscopy (EDS) (Figs. 2f-2i). The overlay of these atom signals shows that RGO and WS_2 are uniformly hybridized to form the 3D macropore walls without any significant aggregation. This structural feature is caused by the large contact area and interplay of two nanosheets triggered by the 2D nanoscale geometry. Our findings related to the morphologies of 3D RWhs are in good agreement with our observations of 3D RMhs (see Fig. S6), which implies that the suggested chemistry is both valid and versatile.

The chemical structure and composition of 3D RWhs were studied by X-ray diffraction (XRD), Raman spectroscopy, X-ray photoelectron spectroscopy (XPS), and thermogravimetric analysis (TGA). Two characteristic XRD peaks at $2\theta = 14.4$ and 24.5, corresponding to the (002) planes of WS_2 and RGO, respectively, identify both types of nanosheets used in the 3D architecture (see Fig. S3). As verified by no peak shifting in the XRD spectra of RGO and WS_2, two nanosheets were neither intercalated into the layers of their counter partner nor were they further exfoliated along the z axis. Raman spectra can be also used to analyze the exfoliated structure of hetero-nanosheets; the frequency difference between the E_{2g} and A_{1g} modes and the intensity of the A_{1g} mode allow for interpretation of the layer thickness and the identification of WS_2.[1,31] Because a single or a few layers of WS_2 show a frequency difference less than 65 cm^{-1} (smaller than the 70 cm^{-1} difference found in the bulk WS_2), the fact that we observed a frequency difference of 60 cm^{-1} indicates that WS_2 nanosheets were well-exfoliated and did not significantly restack after the construction of a 3D structure (Fig. 2j). This was also the case for 3D RMhs. The chemical identities of the 3D RWhs were confirmed by C 1s, O 1s, W 4f, and S 2p XPS spectra corresponding to the characteristic peaks of RGO and WS_2 (Fig. 2k and see Figs. S7, S8). The composition of the 3D RWhs was determined to be a nearly equal ratio of WS_2 and RGO, which is very close to initial mixing ratio, as evaluated by TGA data (Fig. 2l and see Figs. S11, S12).

The interaction between RGO and WS_2 was observed by W 4f and S 2p XPS and Raman spectra (see Supporting Information S5). As shown in the appearance of W-O bonding that was not observed by

bulk and 2D WS_2, the 3D RWhs led to the distinct electronic environments due to the interplay between RGO and WS_2. This observation was analogous to the previous result of RGO/MoS_2 hybrids.[32] I_D/I_G values of GO increased after the hybridization with WS_2, indicating the formation of defects arising from the W-O bonding. The existences of interacting RGO/WS_2 hetero-nanosheets were associated with the increase in the thermal stability of RGO (see Fig. S11) and the inhibition of phase transformation from 1T into 2H phase after the annealing at 200 ^{o}C (see Figs. S23, S24). The EXAFS data also confirmed the presence of W-O bonds, which further confirmed our observation for the existence of interaction between WS_2 and functional groups of RGO (Fig. 4c). This interplay between the oxygen-functional groups of RGO and WS_2 is promoted by the electronic coupling and large contact area of two nanosheets characteristic in the 2D geometry. Since the size, thickness, and surface chemistry of 2D nanosheets can affect the interaction, systematic experiment needs to be performed to understand the detailed mechanism of interaction between WS_2 and RGO, which is beyond the scope of this work.

In this work, highly reversible and ultrafast surface redox charge storage of WS_2-based hybrids was first realized and originated from the interplay between hetero-nanosheets and the hierarchical architectures. The capacitive behaviors of the 3D RWhs were evaluated by cyclic voltammetry (CV) and galvanostatic charge/discharge (GCD) curves as shown in Figure 3. The electrolyte used was a 1 M H_2SO_4 aqueous solution in a three-electrode configuration. We used 2D and 3D RGO films and 2D RWhs as control samples. As shown in the CV curves at 5 mV/s (Fig. 3a), 2D and 3D RGOs exhibited a rectangular shape which is close to a near-ideal double layer capacitive feature in the potential window between -0.3 V and 0.3 V.[33] As the scan rate increased, CV curves of 2D WS_2 were highly distorted and redox waves were not observed at given scan rates due to high overpotential. The effect of the hetero-composition on the capacitive behavior was validated by the enhanced capacitance and enlarged electrochemical window between -0.3 V to 0.4 V (Fig. 3a). As the sweep rate increased from 5 mV/s to 100 mV/s, the CV curves of the 2D RGO and RWhs showed a few deviations and became somewhat distorted. This is indicative of an increased ionic resistance at higher sweep rates (see Fig. S13).[34] The GCD curves also exhibited the same trend at a high rate (see Fig. S14). By contrast, the 3D RGO and

RWhs retained good capacitive behavior, even at 100 mV/s, due to fast ion transport through the 3D interconnected macropores and fast charge transfer (Fig. 3c and see Figs. S13, S15, S16). In particular, the absence of the redox wave in 2D RWhs might be due to insufficient proton accommodation into the electroactive site which is attributable to the slow ion kinetics at high rates.[25,27] Due to a high density of surface-exposed edges, which offer a large number of accessible active sites for protons,[5,6] 3D RWhs exhibited an obvious redox wave at -0.14 V during a cathodic reaction. This is associated with the reversible transition from W^{4+} to $W^{(4-\Delta)+}$ even at a rate of 100 mV/s. Despite the pseudocapacitive feature, the 3D RWhs showed a fast charging/discharging rate comparable to double layer capacitive 3D RGO. To quantitatively evaluate the capacitance and rate capability, the specific capacitances of the electrodes were measured using CV curves. The specific capacitance of the 3D RWhs at 5 mV/s (299 F/s) was 200% and 160% greater than 153 F/g and 186 F/g of 2D and 3D RGOs, respectively. This value was also 120% greater than 253 F/g of 2D RWhs with a composition that was identical to the 3D RWhs. The capacitance gap between 2D (113 F/g) and 3D (262 F/g) RWhs became more pronounced when the charge was stored at a high rate of 100 mV/s. By increasing the sweep rate by a factor of 20 (from 5 mV/s to 100 mV/s), the specific capacitances were reduced from 153 F/g to 39 F/g for the 2D RGO, 186 F/g to 140 F/g for the 3D RGO, 253 F/g to 113 F/g for the 2D RWhs, and 299 F/g to 262 F/g for the 3D RWhs (Fig. 3h). Accordingly, the capacitance retention of the 3D RWhs (88 %) was much greater than 25 % and 45 % of 2D RGO and RWhs, respectively, due to the fast ion kinetics and percolated electron transport through 3D interconnected pathways. Despite the pseudocapacitance two-fold greater than the capacitance of double layer capacitive RGO, the 3D RWhs showed higher capacitance retention compared to 75 % of 3D RGO films due to a redox charge transfer facilitated by the interplay of the 2D hetero-nanosheets (Fig. 3g and see Supporting Information S7). The fast charge transfer dynamics observed in capacitor devices during a redox reaction process demonstrate good rate capabilities in 3D RWhs for high power pseudocapacitors (see Figs. S15, S16).

To investigate for more practical applications, the cycle stability was tested with a two-electrode symmetric configuration at 3 A/g during 3000 charge/discharge cycles (Fig. 3i). The capacitance

retention of the 3D RWhs was 94.7 %, which is comparable to double-layer capacitive 2D and 3D RGOs, despite the pseudocapacitive features yielding high initial capacitance (279 F/g). The 2D RWhs revealed a gradual capacitance increase from 149 F/g to 172 F/g over 100 charge/discharge cycles and 98.8 % of this value was maintained up to 3000 cycles. The capacitive enhancement of the 2D RWhs over 100 cycles implies that redox charge storage emerged during the process of long cyclic testing due to the slow ion kinetics which occurs through the tortuous pathways of the 2D films. These results signify that the surface redox chemistry of WS_2 is manifested by the 3D networking structure and the hetero-composition; faradic charge storage can be operated as long as ion diffusion and charge transfer is sufficiently fast to keep pace with a given rate.[25,27]

The surface redox behavior of WS_2 should be further investigated because WS_2 and its composites have previously been used as insertion materials for battery applications.[23,26] As confirmed by the linear correlation of the sweep rate with the peak current (Fig. 3d), the 3D RWhs behaves in a surface-confined manner (as opposed to a diffusion-controlled manner of bulk WS_2 and 2D RWhs) at the redox potential. This indicates an opportunity for fast charging/discharging rates for high power applications. The surface-dominant redox nature of WS_2 was verified by examining changes in the peak voltages and current shifts with respect to the sweep rates (Fig. 3e). The slight cathodic peak shift, small peak separation, and relatively fast current response of 3D RWhs indicate that the total capacity is dominated by a surface-controlled pseudocapacitive behavior (see Supporting Information S8).[27] Moreover, the contribution of capacitive charging to the total stored charge of the 3D RWhs at a low rate of 5 mV/s was estimated by Dunn's method to be 86.5 %.[35] At higher sweep rates of 100 and 500 mV/s, the capacitive contribution increased to 96.6 and 98.5 %, respectively (Fig. 3f and see Fig. S17.). Using Trasati's method,[36] the capacitive contribution over the total stored charges was determined to be 84.5 %, which was in a good line with the value calculated by Dunn's method at low rates (see Fig. S18). The active materials can be translated from diffusion-controlled to surface-dominating charge storage mechanisms when they overcome solid-state diffusion limitation by fast kinetics driven by nanostructuring. For instance, the intercalation stage mechanism of graphite for electrochemical energy

storage can be translated into the double layer capacitive behaviour when it is downscaled into a single-layer graphene.[40] As the thickness of nanosheets increases, solid-state diffusion of ion species into the active sites becomes more prominent for revealing redox reactions. Accordingly, the thickness of nanosheet that can be controlled by the number of layers is very important for revealing surface redox charge storage behavior of WS_2. Although it is very difficult to determine the critical number of thickness where surface redox reaction starts to occur at given scan rates, we confirmed that the number of layers below 5 showed fast and reversible surface redox reaction as long as WS_2 is hybridized with RGO and architectured in 3D structure.

The charge storage mechanism of the 3D RWhs through the surface redox process was investigated by *in-situ* Raman spectroelectrochemistry as shown in Figure 4. Since the Raman spectra of WS_2 consist of E_{2g} (in-plane displacements involving both of W and S atoms) and A_{1g} (out-of-plane vibrations involving only S atoms) bands,[33] the interaction of the electronic structure with ions during a capacitive charging/discharging process can be monitored by an *in-situ* cell (see Fig. S25 and Supporting Information S11). E_{2g} bands of 3D RWhs gradually shift towards a lower wavenumber as protons are inserted, whereas A_{1g} bands are negligibly shifted (Fig. 4a). The proton insertion into the in-plane W-S lattice of the 3D RWhs enables the E_{2g} bands to soften due to the interplay between the WS_2 and the ions as the potentials vary from 0.4 V to -0.3 V. In contrast, 2D RWhs shows a continuous shift in both the E_{2g} and the A_{1g} bands towards a lower wavenumber during proton insertion (see Fig. S26). This discrepancy in the Raman spectra was attributed to the different dimensional features and assembly mechanisms of the 2D and 3D RWhs. The compact layer-by-layer stacking morphology of 2D RWhs causes both in-plane and out-of-plane Raman vibrations to become active in a redox potential as long as protons are deeply diffused into the redox-active sites between WS_2 layers at very low rates.[37] On the other hand, surface-exposed mono- or few-layers of WS_2 that are uniformly distributed in 3D RWhs enables surface-dominating redox electrochemistry to occur on in-plane W-S (E_{2g}) sites, resulting in a negligible change in the out-of-plane vibrations. Consequently, no redox event of the 2D RWhs was observed at a given rate due to the diffusion limitation into the compactly stacked layers. As the protons

are deserted, 3D RWhs exhibits the same band shift trend as a proton insertion but in the opposite direction (Fig. 4b). The variation of the band position is attributed to the different electronic environments of WS_2 interacting with protons under applied potentials. This is due to the fact that electron/phonon interactions are influenced by the lattice distortion of WS_2 during proton injection/extraction processes. As demonstrated by the change in the Raman active D- and G-modes of RGO (see Fig. S27), the pseudocapacitive charge storage generated by WS_2 was dominant in 3D RWhs. Moreover, the highly reversible charge storage of 3D RWhs is demonstrated by the nearly complete recovery of Raman band positions even after 3000 charge/discharge cycles.

For a deeper understanding of the charge storage mechanism, the changes in the local structure around W atomic element and oxidation state during the capacitive charging/discharging is analyzed by *in-situ* synchrotron X-ray absorption spectroscopy (XAS) (see Supporting Information S12). As shown in the extended X-ray absorption fine structure (EXAFS), three characteristic WS_2 peaks are assigned to the interatomic distances of W-W (2H trigonal prismatic structure), W-W (1T octahedral structure), W-S, and W-O bonds at 3.10, 2.73, 2.02, and 1.26 Å, respectively (Figs. 4c, 4d). By varying the applied potential from 0.3 V to -0.12 V, no significant changes were detected in the W-S and W-O bonds. On the other hand, the 1T peak broadens up to -0.12 V due to proton insertion and shifts with the stretching of W-W bond length. At the fully proton-inserted state, the protons are stabilized and W-W distance is adjusted to make 1T phase, in which the redox reaction mainly occurs, dominant. Then, the material almost returns to the original 1T and 2H peak positions and shape during a proton deinsertion when equilibrium is reached at 0.3 V. When protons are inserted during a cathodic reaction, the interatomic distances of the 1T and 2H phases increase from 2.73 to 2.76 Å and from 3.10 to 3.16 Å, respectively, despite the fact that there is no appreciable change in the W-S bond. The increased distance and intensity change of the W-W bond implies that the redox transition takes place on the surface-exposed intralayers of W-W atoms within an electrochemically active 1T phase of WS_2. Similar findings were observed when Li^+ was fully intercalated at a very low rate for battery applications.[25,27] During the proton deinsertion process, the 1T peak again changes up to -0.12 V and then, is almost entirely

recovered to the same peak position and intensity when compared to samples that did not undergo an applied potential. When the applied potentials vary from -0.3 V to 0.3 V, the interatomic distances of the 1T and 2H phases decrease from 2.76 to 2.73 Å and from 3.16 to 3.10 Å, respectively, and then, return to original state and position after obtaining equilibrium at 0.3 V, which is consistent with samples that did not undergo an applied potential. In particular, a reversible redox transition is coupled with a phase transition from 2H through 1T to the original phase during a pseudocapacitive charging/discharging process. As evaluated by the peak intensity of 1T and 2H phases, the WS_2 of 3D RWhs is composed of two phases in an aqueous electrolyte: 51.7% of 1T and 48.3% of 2H phases. Interestingly, the amount of the distorted 1T phase increases from 51.7% to 74.2% at -0.3 V during a proton insertion. As protons are completely extracted during a proton deinsertion, the distorted structure of 3D RWhs is recovered at 0.3 V. The material is fully restored and converts back to its original structure consisting of 1T (50.3%) and 2H (49.7%) phases.

All the processes are so reversible that the peak transition and full recovery can occur during proton insertion/deinsertion processes. As verified by EXAFS data, both W-W interatomic distances and compositions of the 1T and 2H phases are reversibly changed by the stretching and shrinking of bonding lengths with a phase transition during a redox charging/discharging process. These reversible local geometric change for the proton behavior can be supported with X-ray absorption near edge structure (XANES) spectra in the viewpoint of the oxidation state (Figs. 4e, 4f). During a proton insertion into WS_2 at -0.3 V, the oxidation state systematically changes from W^{4+} to $W^{(4-x)+}$ (most probably to W^{3+}) with respect to the cell potential. This transition was clearly observed by the shift of the rising edge towards a lower energy. When the potentials are changed in the opposite order from -0.3 V to 0.3 V, the oxidation state of WS_2 is transformed from $W^{(4-x)+}$ to W^{4+} through proton deinsertion and is recovered to the original state.

The surface-dominant redox charge storage mechanism of the 3D RWhs is proposed below (Figs. 1b, 4g). Protons are readily accommodated through 3D continuous macroporous pathways and rapidly transported into the electroactive sites of the exposed 1T WS_2 phase on the 3D RWhs during a redox

transition (Fig. 1b). The fast ion transport into the electrode surface is a crucial step to trigger the surface dominating redox electrochemistry at high rates, which is attributed to the unique macroscopic structure of 3D RWhs as confirmed by electrochemical analyses (Fig. 3). Even at the identical composition to 3D RWhs, 2D RWhs fails to yield redox charge storage at a given rate. The redox reaction of 2D RWhs is inhibited due to the diffusion limitation of protons through the tortuous pathways present in the compactly layered structure. Such a structural discrepancy results in different modes of lattice vibrations (Figs. 4a, 4b and see Fig. S24). The differences in electrochemical performance and lattice vibration between 2D and 3D RWhs emphasize the importance of rapid ion transport inside hierarchical architectures for the emergence of surface redox transitions (Fig. 1b). While protons are accommodated onto the in-plane W-S sites of the 3D RWhs, both 1T and 2H phases are distorted and strained during proton insertion; E_{2g} bands are softened due to the interplay of the S atoms in the octahedral WS_2 lattice with the protons (1 in Fig. 4g). As shown in the Raman spectroscopy (Fig. 2j) and XPS (Fig. 2k) results, the thermodynamically-stable 2H phase is converted into the meta-stable 1T phase during exfoliation and thus, 2D WS_2 and hybrids consist of mixed 1T and 2H phases (see Supporting Information S9).[37] Interestingly, a reversible structural change during a redox charging/discharging process under the applied potentials (0.3 V → -0.3 V → 0.3 V) was confirmed by the composition variation from 2H through 1T to the original phase (51.7% → 74.2% → 50.3%) and W-W interatomic distance (2.73 Å → 2.76 Å → 2.73 Å) of 1T phase as verified by XAS data (Fig. 4c). Although the metallic 1T phase is more electrocatalytic active than the semiconducting 2H phase,[5,38] both W-W interatomic distance and composition of the 1T phase are reversibly changed by the stretching and shrinking of bonding lengths during a redox charging/discharging process (2 in Fig. 4g). Importantly, the transition of 2H to 1T phase (i.e. the decrease of the 2H peak intensity and the increase and broadening of the 1T peak intensity at -0.12 V) is observed at both partially anodic and cathodic states during the redox transition (Figs. 4c, 4d). This transition behavior at -0.12 V, where the redox peak in CV curve is emerged, is coupled with the significant change in the oxidation state. In order to satisfy the charge neutrality after the interaction of S atoms with protons, the oxidation state of W atoms

in the octahedral 1T phase is converted from W^{4+} to $W^{(4-x)+}$ during proton insertion (3 in Fig. 4g). As verified by the change in the oxidation state, highly reversible and ultrafast surface redox charge storage of 3D RWhs is accomplished following the reaction route (Figs. 4e, 4f): $WS_2 + xH^+ + xe^- = WS_2H_x$ (in this study, x=0.91 from XANES data). In order to confirm that the octahedral 1T phase acts as the redox active sites, the effect of annealing on the phase transformation is correlated with the variation in the capacitances (see Supporting Information S10). The clear decrease in current density and weakening of redox peaks in the annealed 3D RWhs is observed after the phase transition from 1T to 2H phase, which highlights the importance of 1T structure for redox reactivity. Since the electrochemically active 1T phase is meta-stable and electrically resistive,[37] its interplay with the conductive RGO provides a synergistic effect on the surface redox electrochemistry as demonstrated by the facilitated interfacial charge transfer (see Supporting Information S7) and the stabilization of 1T WS_2 nanosheets *via* the electron donating nature of the oxygen-functional groups of RGO (see Supporting Information S9, S10).[39] As a consequence of the close contact of interacting nanosheets, electrons are rapidly transported through the conducting pathways of RGO and into and out of the redox active sites of WS_2 during charge injection (or proton insertion) and separation (or proton deinsertion) (Fig. 1b).

Next, we discuss the unusual improvement in the capacitive performance of 3D RWhs following three main lines of thought. First, the hierarchical structure consisting of 3D macroporous architectures assembled by 2D hetero-nanosheets provides remarkable electrochemical properties for 3D RWhs; these materials showed greater capacitance and higher rate capability compared to 2D RGO and RWhs due to their large accessible areas and fast ion transport. Second, the hetero-composition of RGO and WS_2 offers the opportunity for synergistic integration of two nanosheets with different electrochemical properties; the incorporation of WS_2 into RGO leads to increased charge storage through the faradaic surface redox process while maintaining rate and cyclic capabilities due to the fast charge transfer and electrochemical integrity. Third, the 2D nanoscale geometry and the interplay of hetero-nanosheets resulted in the homogeneous distribution of surface-exposed WS_2 nanosheets, close contact between RGO and WS_2, fast redox charge transfer, and electrochemical and structural integrity. As the graphene

is exfoliated into a single or few layers, the electrochemical behavior is transformed from diffusion-limited intercalation (which is observed in a bulk graphite) into a surface-dominant double layer capacitive mechanism.[40] Analogously, surface-exposed WS_2 nanosheets show surface-confined redox charge transfer as long as the kinetics of electronic and ionic transport are fast enough to keep pace with the charge/discharge rate.[25,27] This finding is supported by the observation that the capacitance gap between 2D and 3D RWhs was reduced at very slow sweep rates; in this scenario, the given time was long enough to fully diffuse protons into the active sites of the 2D electrode. Thus, the contribution of redox charge storage to the total stored charge of 2D RWhs was enhanced (see Supporting Information S7). Moreover, the redox charge storage of the 2D RWhs was emerged during long cyclic testing due to the slow ion kinetics through the tortuous pathways of the layered structure. Therefore, 2D RWhs at a composition identical to the 3D RWhs failed to show the redox wave at a high rate. Considering that the electrons generated by the redox reaction are readily transported through percolating pathway of RGOs in close contact with the WS_2 nanosheets for both 2D and 3D RWhs, proton accommodation to the redox-active sites of WS_2 is critical for triggering surface redox characteristics. These structural and compositional features of 3D RWhs resulted in the highly reversible and ultrafast surface redox behavior, which has not been observed in either 2D RWhs (in this study) or bulk WS_2 (in previous reports).

In conclusion, we have demonstrated unique surface dominant charge storage mechanism of the two 2D nanomaterials interacting in 3D hierarchical architectures (which is limited only to the electrochemical behavior of the material but can be applied to many other important applications as well) via *in-situ* XAS and Raman techniques. This redox capacitive behavior was attributed to the interplay of the 2D geometry and the coupling of different properties in a synergistic manner. This study provides a fundamental understanding of the unique surface dominating phenomenon of hierarchical hetero-structure and rational design guidelines of emerging electrode materials for high performance electrochemical energy storage devices. Since 3D RWhs consists of mixed phases of both 1T and 2H,

the quantitative contribution of 1T and 2H to the surface redox capacitive behavior will be examined in future work.

Supporting Information.

Additional information on sample synthesis and characterization, experimental section, additional electrochemical and spectroscopic results. This material is available free of charge via the Internet at http://pubs.acs.org.

Acknowledgements

We acknowledge the financial support by the National Research Foundation (NRF) funded by the Ministry of Science, ICT & Future Planning (NRF-2013-220-2013S1A2A2035510). The work done at Brookhaven National Laboratory was supported by the Assistant Secretary for Energy Efficiency and Renewable Energy, Office of Vehicle Technologies of the U.S. Department of Energy (DOE), under contract no. DE-SC0012704.

Author contributions

H. S. P. conceived and led the project and analyzed the data. Q. M. performed experiments of materials synthesis and electrochemistry. M. G. K., S. Y., S. B., and X. Q. Y. performed experiments of synchronous x-ray absorption spectroscopy and analyzed the data. All the authors discussed the results and co-wrote the manuscript.

References

(1) Chhowalla, M.; Shin, H. S.; Eda, G.; Li, L. J.; Loh, K. P.; Zhang, H. The chemistry of two-dimentional layered transition metal dichalcogenide nanosheets. *Nat. Chem.* **2013**, *5*, 263–275.

(2) Xu, M.; Liang, T.; Shi, M.; Chen, H. Graphene-like two-dimensional materials. *Chem. Rev.* **2013**, *113*, 3766–3798.

(3) Liu, J.; Liu, X. W. Two-dimentional nanoarchitectures for lithium storage. *Adv. Mater.* **2012**, *24*, 4097–4111.

(4) Hu, S.; Wang, X. Ultrathin nanostructures: smaller size with new phenomena. *Chem. Soc. Rev.* **2013**, *42*, 5577–5594.

(5) Voiry, D. *et al.*, Enhanced catalytic activity in strained chemically exfoliated WS_2 nanosheets for hydrogen evolution. *Nat. Mater.* **2013**, *12*, 850–855.

(6) Kibsgaard, J.; Chen, Z.; Reinecke, B. N.; Jaramillo, T. F. Engineering the surface structure of MoS_2 to preferentially expose active edge sites for electrocatalysis. *Nat. Mater.* **2012**, *11*, 963–969.

(7) Geim, A. K.; Grigorieva, I. V. Van der Waals heterostructures. *Nature* **2013**, *399*, 419–425.

(8) Hamm, J. M.; Hess, O. Two two-dimentional materials are better than one. *Science* **2013**, *340*, 1298–1299.

(9) Yu, W. J.; Li, Z.; Zhou, H.; Chen, Y.; Wang, Y.; Huang, Y.; Duan, X. Vertically stacked multi-heterostructures of layerecd materials for logic transistors and complementary invertors. *Nat. Mater.* **2013**, *12*, 246–252.

(10) Gao, G. *et al.*, Artificially stacked atomic layers: toward new van der waals solids. *Nano Lett.* **2012**, *12*, 3518–3525.

(11) Britnell, L. *et al.*, Strong light-matter interactions in heterostructures of atomically thin films. *Science* **2013**, *340*, 1311–1314.

(12) Hong, X. *et al.*, Ultrafast charge transfer in atomically thin MoS_2/WS_2 heterostructures. *Nat. Nanotech.* **2014**, *9*, 682–686.

(13) Fang, H. *et al.*, Strong interlayer coupling in van der Waals heterostructures built from single-layer chalcogenides. *Proc. Natl. Acad. Sci.* **2014**, *111*, 6198–6202.

(14) Yankowitz, M.; Xue, J.; Cormode, D.; Sanchez-Yamagishi, J. D.; Watanabe, K.; Taniguchi, T.; Jarillo-Herrero, P.; Jacquod, P.; LeRoy, B. J. Emergence of superlattice Dirac points in graphene on hexagonal boron nitride. *Nat. Phys*. **2012**, *8*, 382–386.

(15) Hunt, B. *et al.*, Massive Dirac fermions and Hofstadter butterfly in a van der Waals heterostructure. *Science* **2013**, *340*, 1427–1430.

(16) Dean, C. R. *et al.*, Hofstadter's butterfly and the fractal quantum Hall effect in moiré superlattices. *Nature* **2013**, *497*, 598–602.

(17) Chen, Z.; Ren, W.; Gao, L.; Liu, B.; Pei, S.; Cheng, H. M. Three-dimensional flexible and conductive interconnected graphene networks grown by chemical vapour deposition. *Nat. Mater*. **2011**, *10*, 424–428.

(18) Rolison, D. R.; Long, J. W.; Lytle, J. C.; Fischer, A. E.; Rhodes, C. P.; McEvoy, T. M.; Bourg, M. E.; Lubers, A. M. Multifunctional 3D nanoarchitectures for energy storage and conversion. *Chem. Soc. Rev.* **2009**, *38*, 226–252.

(19) Mann, S. Self-assembly and transformation of hybrid nano-objects and nanostructures under equilibrium and non-equilibrium conditions. *Nat. Mater.* **2009**, *8*, 781–792.

(20) Wang, P.; Sun, H.; Ji, Y.; Li, W.; Wang, X. Three-dimensional assembly of single-layered MoS_2. *Adv. Mater.* **2014**, *26*, 964–969.

(21) Zhang, H.; Yu, X.; Braun, P. V. Three-dimentional bicontinuous ultrafast-charge and-discharge bulk battery electrodes. *Nat. Nanotech.* **2011**, *6*, 277–281.

(22) Feng, J.; Sun, X.; Wu, C.; Peng, L.; Lin, C.; Hu, S.; Yang, J.; Xie, Y. Metallic few-layered VS_2 ultrathin nanosheets: high two-dimensional conductivity for in-plane supercapacitors. *J. Am. Chem. Soc.* **2011**, *133*, 17832–17838.

(23) Chen, D.; Ji, G.; Ding, B.; Ma, Y.; Qu, B.; Chen, W.; Lee J. Y. In situ nitrogenated graphene-few-layer WS_2 composites for fast and reversible Li^+ storage. *Nanoscale* **2013**, *5*, 7890–7896.

(24) Simon, P.; Gogotsi, Y. Materials for electrochemical capacitors. *Nat. Mater.* **2008**, *7*, 845–854.

(25) Conway, B. E. Transition from "supercapacitor" to "battery" behavior in electrochemical energy storage. *J. Electrochem. Soc.* **1991**, *138*, 1539–1548.

(26) Liu, H.; Su, D.; Wang, G.; Qiao, S. Z. An ordered mesoporous WS_2 anode material with superior electrochemical performance for lithium ion batteries. *J. Mater. Chem.* **2012**, *22*, 17437–17440.

(27) Augustyn, V.; Come, J.; Lowe, M. A.; Kim, J. W.; Taberna, P. L.; Tolbert, S. H.; Abruña, H. D.; Simon, P.; Dunn, B. High-rate electrochemical energy storage through Li^+ intercalation pseudocapacitance. *Nat. Mater.* **2013**, *12*, 518–522.

(28) Zhao, X.; Sanchez, B. M.; Dobson, P. J.; Grant, P. S. The role of nanomaterials in redox-based supercapacitors for next generation energy storage devices. *Nanoscale* **2011**, *3*, 839–855.

(29) Nicolosi, V.; Chhowalla, M.; Kanatzidis, M. G.; Strano, M. S.; Coleman, J. N. Liquid exfoliation of layered materials. *Science* **2013**, *340*, 1226419-1–1226419-18.

(30) Hummers, W. S.; Offeman, R. E. Preparation of graphitic oxide. *J. Am. Chem. Soc.* **1958**, *80*, 1339–1339.

(31) Berkdemir, A. *et al.*, Identification of individual and few layers of WS_2 using Raman spectroscopy. *Sci. Reports* **2013**, DOI: 10.1038/srep01755.

(32) Firmiano, E. G. da S.; Rabelo, A. C.; Dalmaschio, C. J.; Pinheiro, A. N.; Pereira, E. C.; Schreiner, W. H.; Leite, E. R. Supercapacitor electrodes obtained by directly bonding 2D MoS_2 on reduced graphene oxide. *Adv. Energy. Mater.* **2014**, *4*, 13013801–13013808.

(33) Choi, B. G.; Hong, J.; Hong, W. H.; Hammond, P. T.; Park, H. S. Facilitated ion transport in all-solid-state flexible supercapacitors. *ACS Nano* **2011**, *5*, 7205–7213.

(34) Kaempgen, M.; Chan, C. K.; Ma, J.; Cui, Y.; Gruner, G. Printable thin film supercapacitors using single-walled carbon nanotubes. *Nano Lett.* **2009**, *9*, 1872–1876.

(35) Wang, J.; Polleux, J.; Lim, J.; Dunn, B. Pseudocapacitive contributions to electrochemical energy storage in TiO_2 (Anatase) nanoparticles. *J. Phys. Chem. C* **2007**, *111*, 14925–14931.

(36) Ardizzone, S.; Fregonara, G.; Trasatti, S. "Inner" and "outer" active surface of RuO_2 electrodes. *Electrochim. Acta* **1990**, *35*, 263–267.

(37) Eda, G.; Yamaguchi, H.; Voiry, D.; Fujita, T.; Chen, M.; Chhowalla, M. Photoluminescence from chemically exfoliated MoS_2. *Nano Lett.* **2011**, *11*, 5111–5116.

(38) Ataca, C.; Sahin, H.; Ciraci, S. Stable, Single-layer MX_2 transition-metal oxides and dichalcogenides in a honeycomb-like structure. *J. Phys. Chem. C* **2012**, *116*, 8983–8999.

(39) Enyashin, A. N.; Yadgarov, L.; Houben, L.; Popov, I.; Weidenbach, M.; Tenne, R.; Bar-Sadan, M.; Seifert, G. New route for stabilization of 1T-WS_2 and MoS_2 phases. *J. Phys. Chem. C* **2011**, *115*, 24586–24591.

(40) Pollak, E.; Geng, B.; Jeon, K. J.; Lucas, I. T.; Richardson, T. J.; Wang, F.; Kostecki, R. The interaction of Li^+ with single-layer and few-layer graphene. *Nano Lett.* **2010**, *10*, 3386–3388.

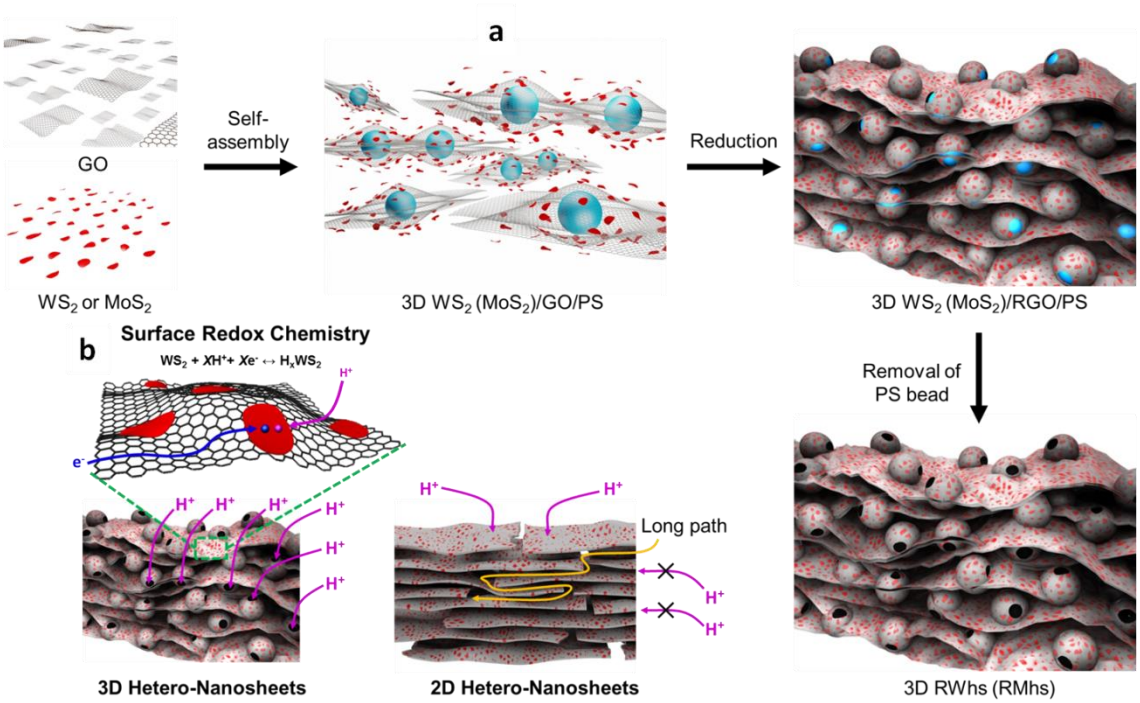

Figure 1. Schematic illustration of the synthesis procedures for 2D hetero-nanosheets assembled 3D hierarchical architectures and the charge storage mechanism of 3D RWhs. (a) Solution-based synthesis of 3D RWhs (or 3D RMhs) through the exfoliation of GO and WS_2 (or MoS_2), the self-assembly with positively charged PS beads, the reduction into 3D WS_2/RGO/PS (or MoS_2/RGO/PS), and the removal of PS beads by solvent extraction. (b) Surface dominating redox transition of 3D RWhs with electron transport through the conduction pathways of RGO and the proton insertion through the 3D macroporous pathways. No redox reaction of 2D RWhs is observed at high rates due to the diffusion limitations of the protons.

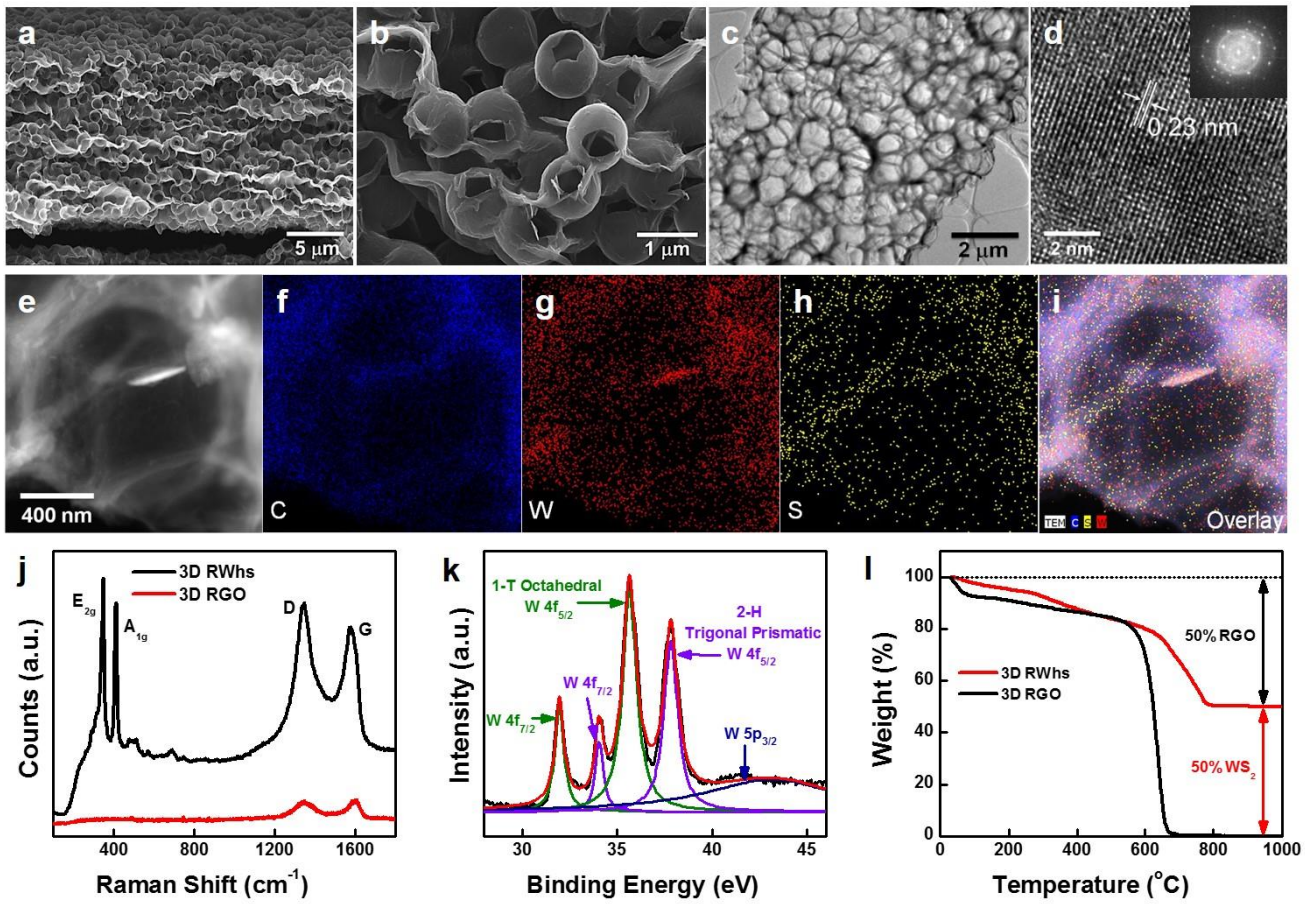

Figure 2. Structural characterization and compositional analysis of 3D RWhs. (a) and (b) SEM images of 3D RWhs at low and high magnifications. (c) and (d) TEM and HR-TEM images of 3D RWhs. Inset of D is the FFT pattern of the corresponding HR-TEM image. (e)−(i) HAADF-STEM image and its corresponding EDS elemental mappings of 3D RWhs. (j) Raman spectra of 3D RGO and RWhs samples. (k) XPS spectra of 3D RWhs. (l) TGA analysis curves of 3D RGO and RWhs samples.

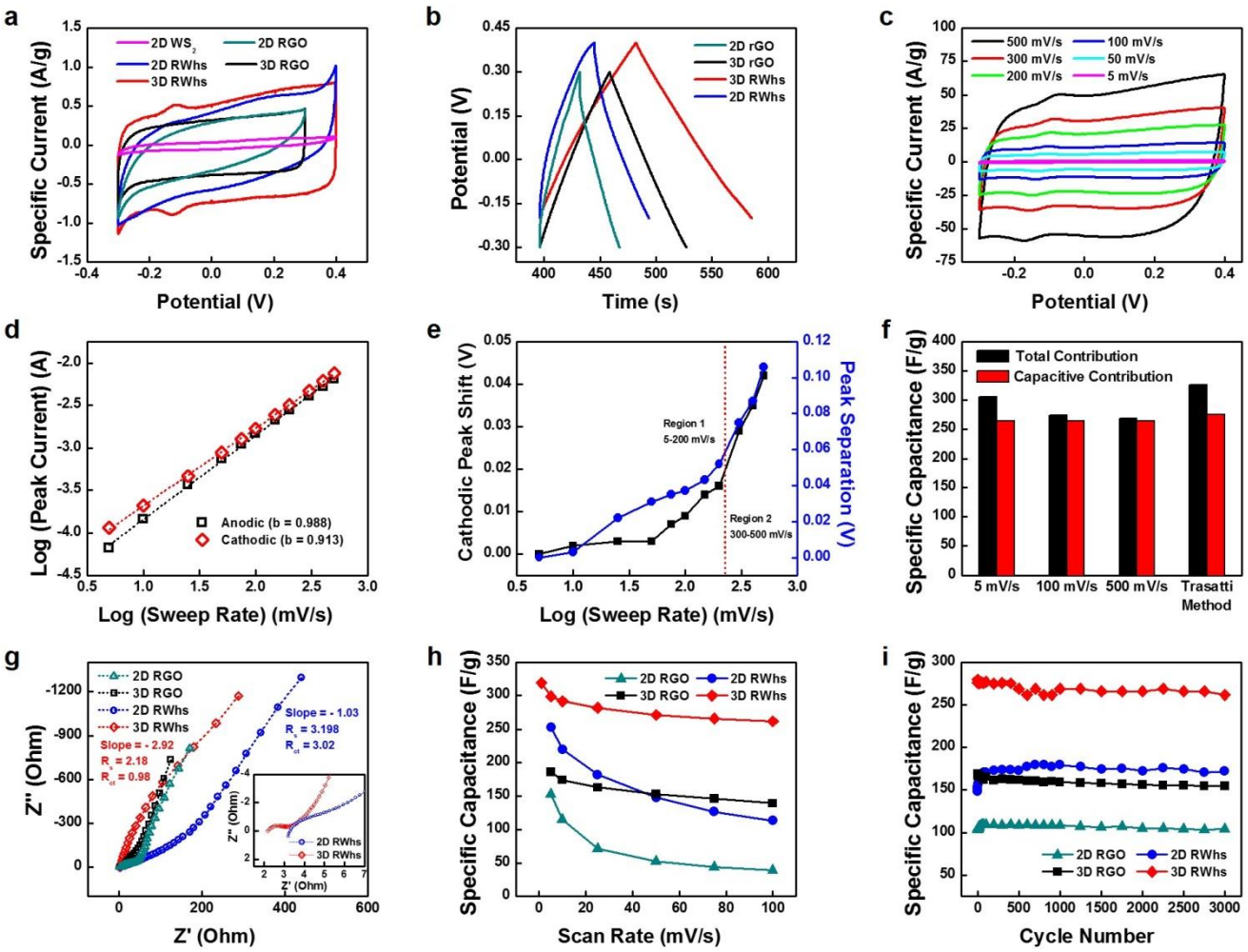

Figure 3. Electrochemical and pseudocapacitive behaviors of 3D RWhs. (a) CV curves of 2D WS_2, 2D RGO, 2D RWhs, 3D RGO, and 3D RWhs at a scan rate of 5 mV/s. (b) GCD plots of 2D RGO, 2D RWhs, 3D RGO, and 3D RWhs at a specific current of 1 A/g. (c) CV curves of 3D RWhs at scan rates between 5 mV/s and 500 mV/s. (d) Plots of log sweep rate vs. anodic and cathodic peak current for the calculation of b values of 3D RWhs. (e) Plots of log sweep rate vs. cathodic peak shift and log sweep rate vs. peak separation of 3D RWhs. (f) Capacitive and diffusive contributions to the total stored charge of 3D RWhs. (g) Nyquist plots of 2D RGO, 2D RWhs, 3D RGO, and 3D RWhs. Inset shows magnified plots of the high-frequency region. (h) Rate capabilities of 2D RGO, 2D RWhs, 3D RGO, and 3D RWhs with scan rates varied from 5 mV/s to 100 mV/s. (i) Cyclic performances of 2D RGO, 2D RWhs, 3D RGO, and 3D RWhs during 3000 charging/discharging cycles.

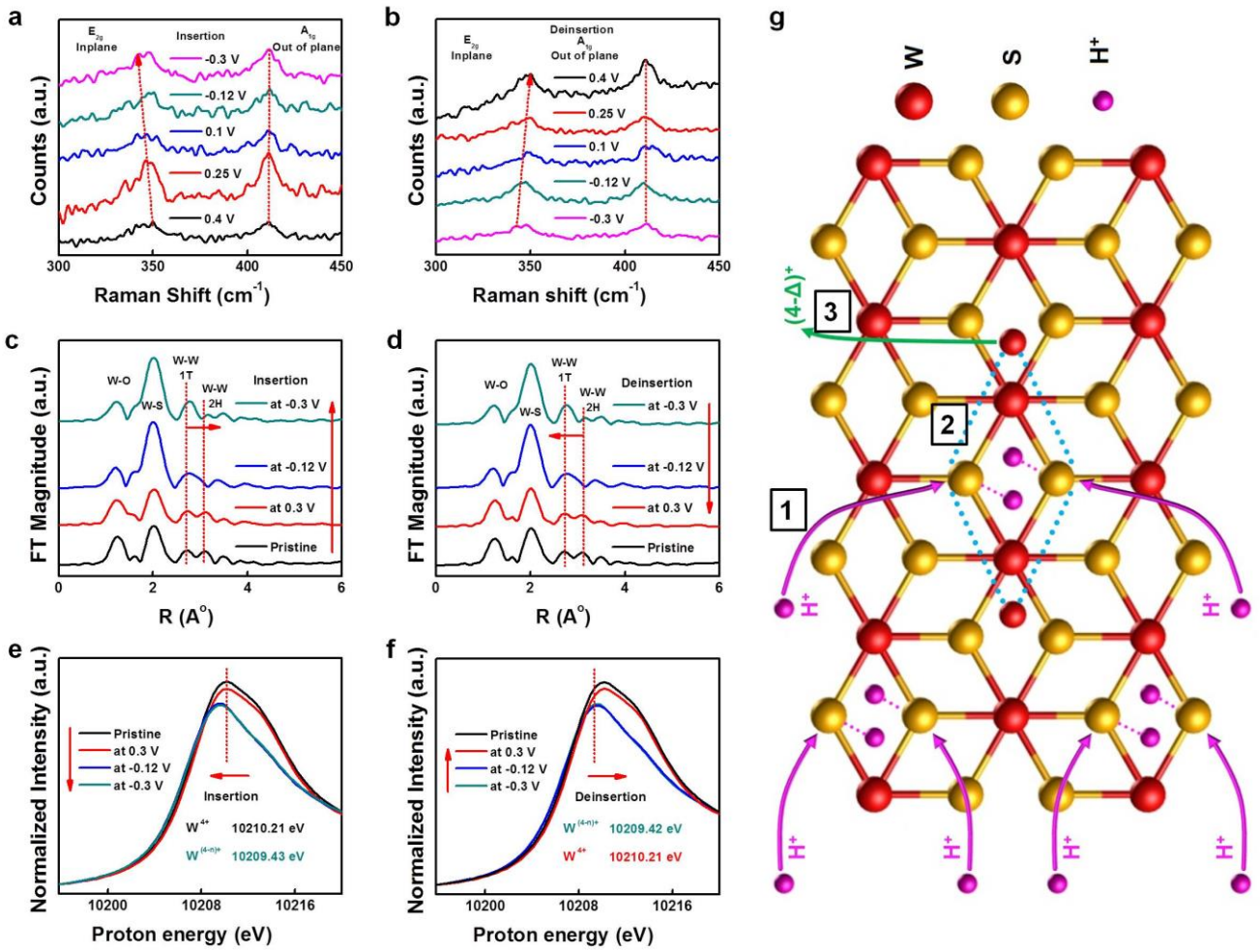

Figure 4. Analysis of surface charge storage mechanism by *in-situ* Raman and XAS spectroelectrochemistries. (a) and (b) *In-situ* Raman spectra at different potentials during proton insertion and deinsertion processes of 3D RWhs. (c) and (d) *In-situ* EXAFS spectra at different potentials during proton insertion and deinsertion processes of 3D RWhs. (e) and (f) *In-situ* XANES spectra at different potentials during proton insertion and deinsertion processes of 3D RWhs. g, Surface redox charge storage mechanism occurring on the octahedral 1T phase structure of WS_2 (paths 1, 2, and 3).

Table of Contents (TOC)

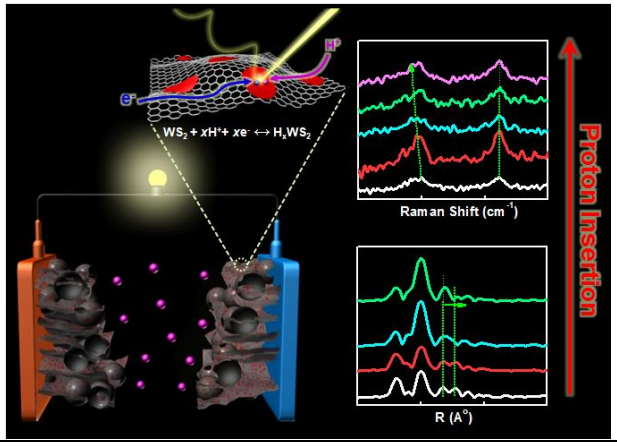

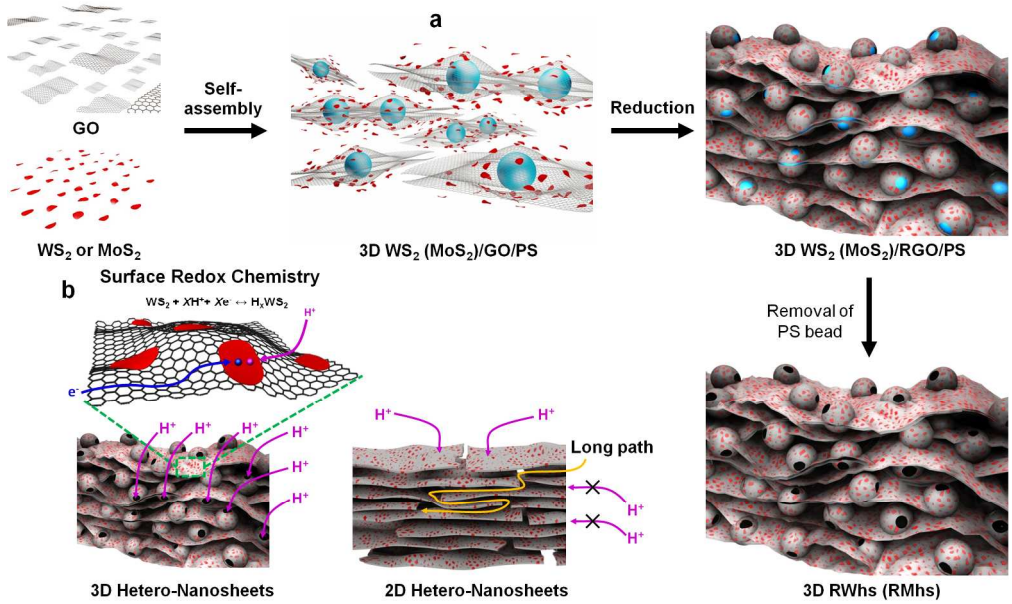

643x390mm (96 x 96 DPI)

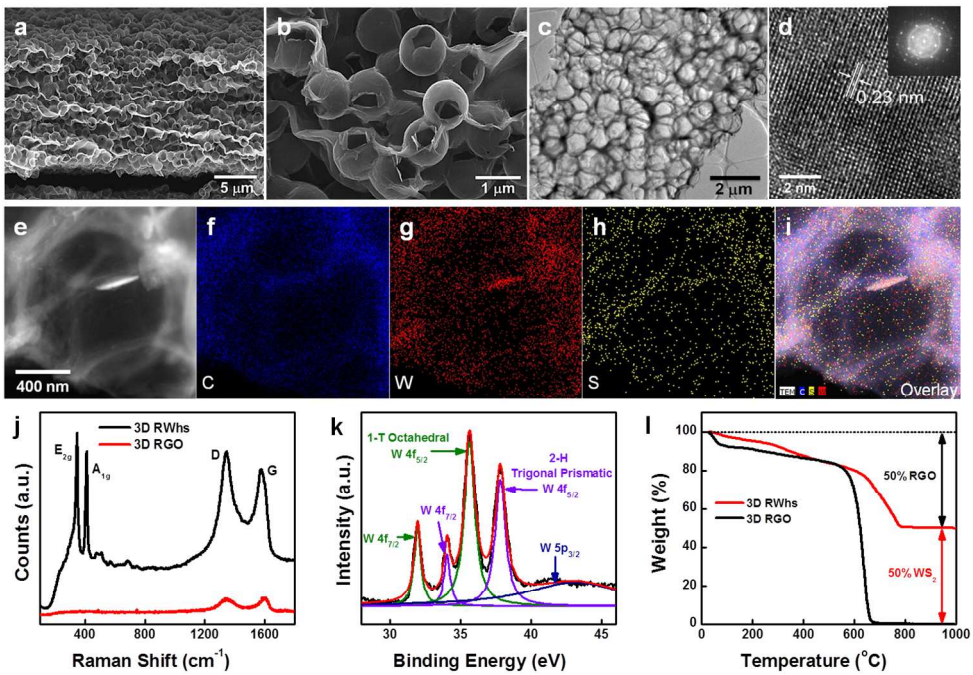

405x278mm (96 x 96 DPI)

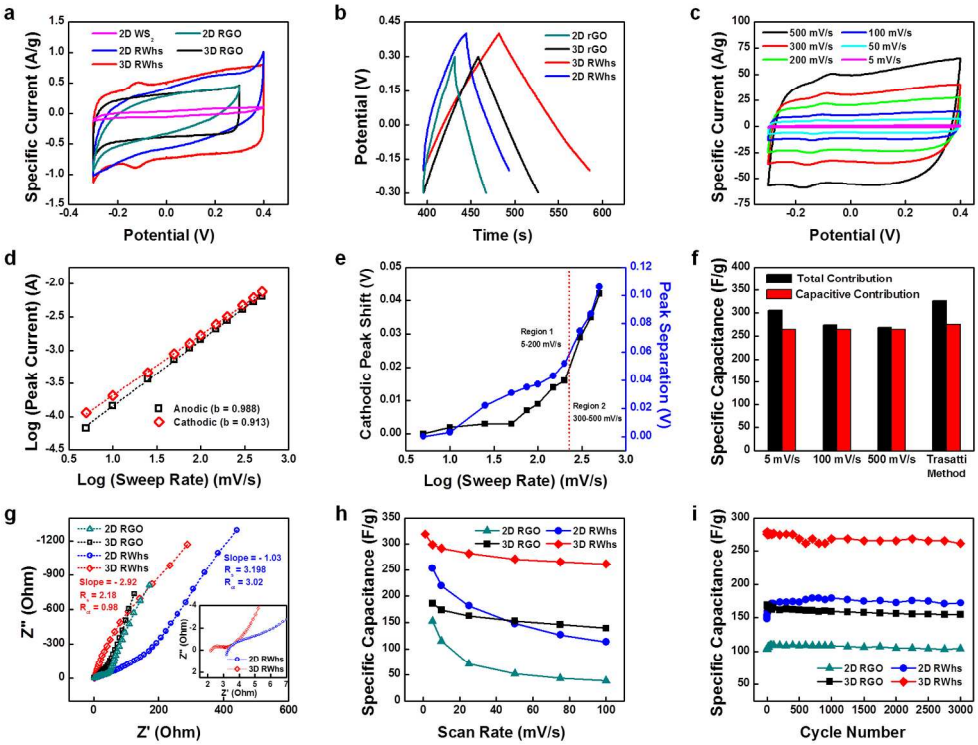

533x406mm (96 x 96 DPI)

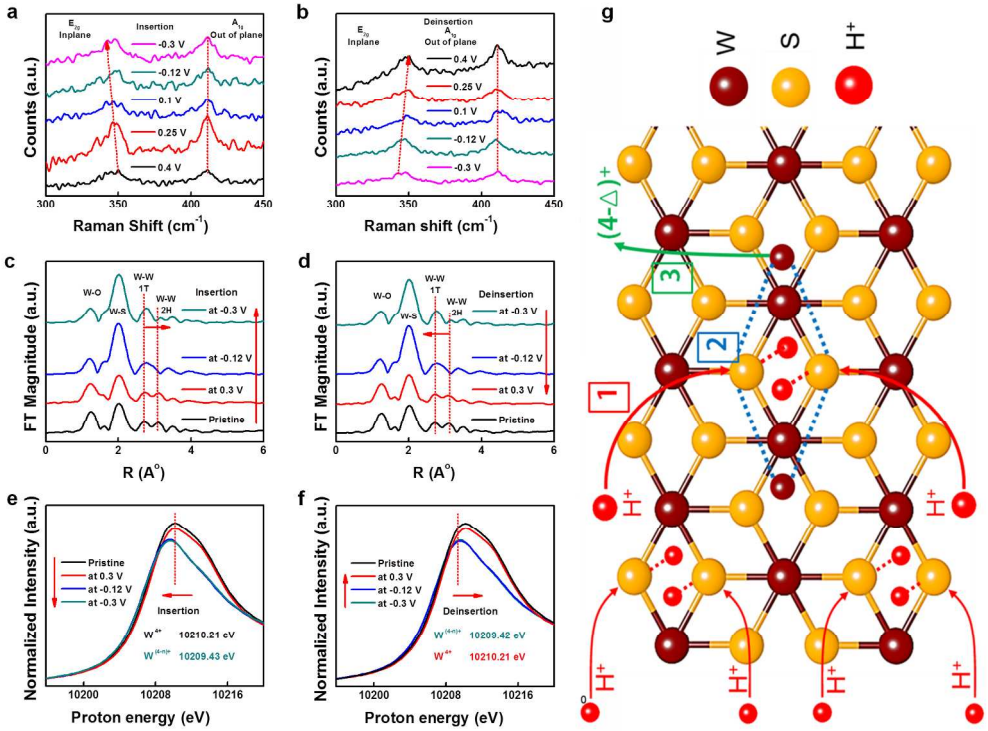

646x484mm (96 x 96 DPI)

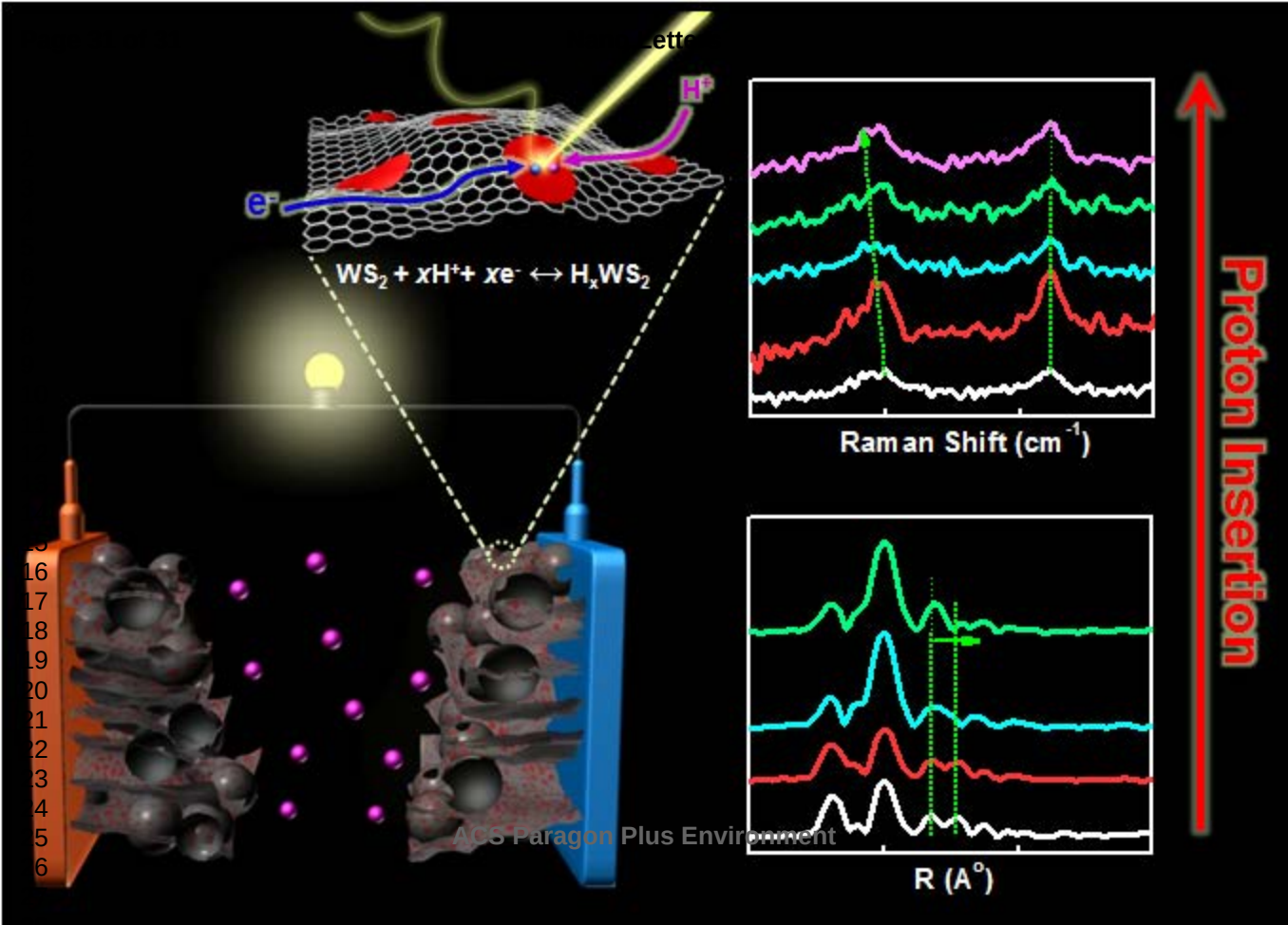

ACS Paragon Plus Environment